Ground-penetrating radar: Wave theory and numerical simulation in lossy anisotropic media

José M. Carcione*

ABSTRACT

Subsurface georadar is a high-resolution technique based on the propagation of high-frequency radio waves. Modeling radio waves in a realistic medium requires the simulation of the complete wavefield and the correct description of the petrophysical properties, such as conductivity and dielectric relaxation. Here, the theory is developed for 2-D transverse magnetic (TM) waves, with a different relaxation function associated to each principal permittivity and conductivity component. In this way, the wave characteristics (e.g., wavefront and attenuation) are anisotropic and have a general frequency dependence. These characteristics are investigated through a plane-wave analysis that gives the expressions of measurable quantities such as the quality factor and the energy velocity. The numerical solution for arbitrary heterogeneous media is obtained by a grid method that uses a time-splitting algorithm to circumvent the stiffness of the differential equations. The modeling correctly reproduces the amplitude and the wavefront shape predicted by the plane-wave analysis for homogeneous media, confirming, in this way, both the theoretical analysis and the numerical algorithm. Finally, the modeling is applied to the evaluation of the electromagnetic response of contaminant pools in a sand aquifer. The results indicate the degree of resolution (radar frequency) necessary to identify the pools and the differences between the anisotropic and isotropic radargrams versus the source-receiver distance.

INTRODUCTION

The applications of ground-penetrating radar (GPR) as an ecological, high-resolution nondestructive technique are widely documented. They include mineral and groundwater exploration (Davis and Annan, 1989), archaeological investigations (Imai et al., 1987; Bevan, 1991), monitoring of oil recovery processes (Witterholt and Kretzschmar, 1984), and engineering applications (Lau et al., 1992). The similarities between high-frequency electromagnetic and seismic wave propagation (Ursin, 1983; Carcione and Cavallini, 1995) allow the application of seismic acquisition and data processing techniques to electromagnetic radar signals (e.g., Fisher et al., 1992).

In particular, forward modeling in heterogeneous media is essential to validate the geological interpretations. Electromagnetic modeling in the hundreds of KHz range (i.e., including the displacement currents) has been applied in Greenfield and Wu (1991) for interpreting field results in disrupted coal seams. However, GPR wave modeling is, in general, one dimensional in the literature. Only very recently, Goodman (1994) proposed a 2-D wave simulation method based on ray-tracing techniques. The modeling is restricted to the isotropic case and suffers the disadvantages of ray methods, i.e., the impossibility to model the full wavefield at all frequency ranges (e.g., the complete set of multiples and diffractions), and the generation of nonuniform dissipative waves at material interfaces. Anisotropy may be found at different scales (Negi and Saraf, 1989): finely stratified layers, compaction, fluid-filled cracks and fractures give rise to anisotropy in electrical and magnetic properties. Since the dielectric constant of water is 80, and that for most dry rocks is in the range 4–8, a set of aligned fluid-filled fractures may present a high degree of dielectric anisotropy. Similarly, the presence of mineralized water (high ionic conductivity) in the fractures produces anisotropy in the electrical conductivity. In some cases, like interbedded shales and sandstones, the longitudinal conductivity can be as far as nine times the transverse conductivity. Moreover, in most crystalline solids like rocks, ice, etc., intrinsic anisotropy occurs because of the preferred arrangement of the atoms and molecules.

Besides the correct description of the anisotropic behavior, it is important to model the frequency dependence of the permittivity and conductivity tensors. At radar frequencies ($\approx$50 MHz–1 GHz), various dielectric dispersion processes occur. In moist soils, the most important are ionic conductivity and bound-water relaxation (Hasted, 1973, 238). The relaxation of the water molecule produces an increase in attenuation

with frequency, since the molecules begin to lag the applied field and increase the real effective conductivity. This phenomenon is well described by a Debye relaxation peak (e.g., Turner and Siggins, 1994). Other, less important processes that can be described by Debye mechanisms, are the Maxwell–Wagner effect and surface conductivity at low frequencies, and the two relaxations of free water at high frequencies (Hasted, 1973). Moreover, at high frequencies, the response of free charges may lag the electric field and produce an out-of-phase component, contributing to the real effective permittivity (Turner and Siggins, 1994).

In this paper, I present a theory that includes anisotropy and dissipation, through the use of permittivity and relaxation tensors in the constitutive relations. By using the acoustic-electromagnetic-mechanical analogy, a set of standard linear solid elements describe several dielectric relaxation mechanisms, and a single Kelvin–Voigt element includes the out-of-phase behavior of the electric conductivity. A different relaxation function is associated with each principal permittivity and each principal conductivity. I assume that the material properties are invariant along, say, the y-direction. Then, the magnetic component H_y and the electric components E_x and E_z are uncoupled from the other three components and the propagation becomes two dimensional [the transverse magnetic (TM) mode]. The physics of the wave propagation is illustrated by probing the medium with a uniform plane wave. The resulting time-domain electromagnetic equations are solved with a direct grid method that computes the spatial derivatives by using the Fourier pseudospectral method and propagates the solution in time with a fourth-order Runge–Kutta algorithm.

MAXWELL'S EQUATIONS FOR GENERAL ANISOTROPIC MEDIA

In 3-D vector notation, the Maxwell equations are (e.g., Chew, 1990)

$$\nabla \times \mathbf{E} = -\frac{\partial \mathbf{B}}{\partial t} + \mathbf{M}, \tag{1}$$

$$\nabla \times \mathbf{H} = \frac{\partial \mathbf{D}}{\partial t} + \mathbf{J}, \tag{2}$$

where $\mathbf{E}$, $\mathbf{B}$, $\mathbf{H}$, and $\mathbf{D}$ are the electric intensity, the magnetic flux density, the magnetic intensity, and the electric flux density, respectively, and $\mathbf{J}$ and $\mathbf{M}$ are the electric and magnetic source current densities, respectively. In general, they depend on (x, y, z), the Cartesian coordinates, and t, the time variable. Equations (1) and (2) constitute six scalar equations with 12 scalar unknowns, since $\mathbf{M}$ is known and $\mathbf{J}$ can be expressed in terms of the electric field. The six additional scalar equations are the constitutive relations, which for anisotropic media including dielectric relaxation, can be written as

$$\mathbf{D} = \underset{\sim}{\epsilon} * \frac{\partial \mathbf{E}}{\partial t}, \tag{3}$$

$$\mathbf{B} = \underset{\sim}{\mu} \cdot \mathbf{H}, \tag{4}$$

where $\underset{\sim}{\epsilon}(\mathbf{x}, t)$ is the permittivity relaxation tensor and $\underset{\sim}{\mu}(\mathbf{x})$ is the permeability tensor. The symbol $*$ denotes time convolution, and the dot on the right-hand side of equation (4) denotes

ordinary matrix multiplication. Moreover, the electric current density is given by the generalized Ohm's law,

$$\mathbf{J} = \underset{\sim}{\sigma} * \frac{\partial \mathbf{E}}{\partial t} + \mathbf{J}_s, \tag{5}$$

where $\underset{\sim}{\sigma}(\mathbf{x}, t)$ is the conductivity relaxation tensor and $\mathbf{J}_s$ is the contribution of the sources. The first term on the right-hand side of equation (5) is the conduction current density, and the convolution accounts for out-of-phase components of the current with respect to the electric field. Substituting the constitutive relations and the current density into equations (1) and (2), and using properties of the convolution, gives

$$\nabla \times \mathbf{E} = -\underset{\sim}{\mu} \cdot \frac{\partial \mathbf{H}}{\partial t} + \mathbf{M}, \tag{6}$$

$$\nabla \times \mathbf{H} = \underset{\sim}{\sigma} * \frac{\partial \mathbf{E}}{\partial t} + \underset{\sim}{\epsilon} * \frac{\partial^2 \mathbf{E}}{\partial t^2} + \mathbf{J}_s, \tag{7}$$

which correspond to a system of six scalar equations in six scalar unknowns.

THE TM WAVE EQUATION

In general, an anisotropic medium is described by symmetric permittivity and conductivity relaxation tensors that can be defined by six components. However, there always exists a coordinate transformation that diagonalizes these symmetric matrices. This transformation is called the principal system of the medium and gives the three principal components of these tensors. In cubic and isotropic media, the principal components are all equal. In tetragonal and hexagonal materials, two of the three parameters are equal. In orthorhombic, monoclinic, and triclinic media, all the three components are unequal.

For the sake of simplicity in the evaluation of the final equations, I consider that the problem is solved in a Cartesian system that coincides with the principal system of the medium. For completeness, the general equations are given, without proof, in Appendix A. In the principal system, the permittivity and conductivity relaxation tensors corresponding to a general anisotropic medium are

$$\underset{\sim}{\epsilon} = \begin{bmatrix} \epsilon_{11} & 0 & 0 \\ 0 & \epsilon_{22} & 0 \\ 0 & 0 & \epsilon_{33} \end{bmatrix} \tag{8}$$

and

$$\underset{\sim}{\sigma} = \begin{bmatrix} \sigma_{11} & 0 & 0 \\ 0 & \sigma_{22} & 0 \\ 0 & 0 & \sigma_{33} \end{bmatrix}, \tag{9}$$

respectively. The permeability tensor is, for most earth materials, isotropic. In this case, it is $\underset{\sim}{\mu} = \mu\mathbf{1}$; here, μ is the scalar permeability and $\mathbf{1}$ is the 3×3 identity matrix.

Now, I assume that the propagation is in the (x, z)-plane, and that the material properties are constant with respect to the y-coordinate. Then, E_x, E_z, and H_y are decoupled from

E_y, H_x, and H_z. The first three fields obey the TM (transverse magnetic field) differential equations:

$$\frac{\partial E_z}{\partial x} - \frac{\partial E_x}{\partial z} = \mu \frac{\partial H_y}{\partial t} - M_y, \tag{10}$$

$$-\frac{\partial H_y}{\partial z} = \sigma_{11} * \frac{\partial E_x}{\partial t} + \epsilon_{11} * \frac{\partial^2 E_x}{\partial t^2} + J_{sx}, \tag{11}$$

$$\frac{\partial H_y}{\partial x} = \sigma_{33} * \frac{\partial E_z}{\partial t} + \epsilon_{33} * \frac{\partial^2 E_z}{\partial t^2} + J_{sz}. \tag{12}$$

The relaxation components

A realistic description of dielectric relaxation can be obtained by representing the principal components with a generalized Debye model. This model accounts for many relaxation mechanisms that produce an out-of-phase component of the permittivity, such as atomic, molecular and volume polarization (King and Smith, 1981). The principal relaxation components can be expressed as

$$\epsilon_{ii}(t) = \epsilon_{ii}^0 \left[1 - \frac{1}{L_i} \sum_{\ell=1}^{L_i} \left(1 - \frac{\lambda_{ii\ell}}{\tau_{ii\ell}} \right) \exp(-t/\tau_{ii\ell}) \right] H(t),$$
$$i = 1 \text{ or } 3, \quad (13)$$

where ϵ_{ii}^0 is the static permittivity, $\lambda_{ii\ell}$ and $\tau_{ii\ell}$ are relaxation times ($\lambda_{ii\ell} \leq \tau_{ii\ell}$), and L_i is the number of Debye relaxation mechanisms; $H(t)$ is the Heaviside function. Actually, the condition $\lambda_{ii\ell} \leq \tau_{ii\ell}$ makes the relaxation function (13) analogous to the viscoelastic creep function of a series connection of standard linear solid elements (e.g., Casula and Carcione, 1992). The optical or high-frequency permittivity is obtained for $t \to 0$. It gives

$$\epsilon_{ii}^\infty = \frac{\epsilon_{ii}^0}{L_i} \sum_{\ell=1}^{L_i} \frac{\lambda_{ii\ell}}{\tau_{ii\ell}}. \tag{14}$$

Note that $\epsilon_{ii}^\infty \leq \epsilon_{ii}^0$ always. On the other hand, the conductivity components are represented by a Kelvin–Voigt mechanical model analog (e.g., Casula and Carcione, 1992):

$$\sigma_{ii}(t) = \sigma_{ii}^0 [H(t) + \xi_{ii}\delta(t)], \qquad i = 1 \text{ or } 3, \tag{15}$$

where σ_{ii}^0 is the static conductivity, ξ_{ii} is a relaxation time, and $\delta(t)$ is the Dirac function. The out-of-phase component of the conduction current is quantified by the relaxation time ξ_{ii}. As shown later, this choice implies a component of the conduction current $90°$ out-of-phase with respect to the electric field.

Introduction of the hidden variables

The TM equations (10), (11), and (12) could be the basis for a numerical solution algorithm. However, the numerical evaluation of the convolution integrals is prohibitive when solving the differential equations with grid methods and explicit time evolution techniques. The conductivity terms pose no problems, since the substitution of the conductivity relaxation components into equations (11) and (12) does not involve time convolutions [see equation (21) below]. To circumvent the convolutions caused by the permittivity components, a new set of field variables is introduced.

Let us consider, for instance, the terms $\epsilon_{ii} * \partial^2 E_m/\partial t^2$ in equations (11) and (12), where $m = 1(x)$ when $i = 1$ and $m = 3(z)$ when $i = 3$. Using equations (13) and (14) and convolution properties[1] yields

$$\epsilon_{ii} * \frac{\partial^2 E_m}{\partial t^2} = \frac{\partial^2 \epsilon_{ii}}{\partial t^2} * E_m = \epsilon_{ii}^\infty \frac{\partial E_m}{\partial t} + \epsilon_{ii}^0 \sum_{\ell=1}^{L_i} \phi_{ii\ell}(0) E_m$$
$$- \epsilon_{ii}^0 \sum_{\ell=1}^{L_i} \frac{1}{\tau_{ii\ell}} \phi_{ii\ell} * E_m, \tag{16}$$

where

$$\phi_{ii\ell}(t) = \frac{H(t)}{L_i \tau_{ii\ell}} \left(1 - \frac{\lambda_{ii\ell}}{\tau_{ii\ell}} \right) \exp(-t/\tau_{ii\ell}),$$
$$\ell = 1, \ldots, L_i. \tag{17}$$

Defining the *hidden* field variables

$$e_{ii\ell} = -\frac{1}{\tau_{ii\ell}} \phi_{ii\ell} * E_m, \qquad \ell = 1, \ldots, L_i, \tag{18}$$

equation (16) takes the form

$$\epsilon_{ii} * \frac{\partial^2 E_m}{\partial t^2} = \epsilon_{ii}^\infty \frac{\partial E_m}{\partial t} + \epsilon_{ii}^0 \left[\Phi_{ii} E_m + \sum_{\ell=1}^{L_i} e_{ii\ell} \right], \tag{19}$$

where

$$\Phi_{ii} = \sum_{\ell=1}^{L_i} \phi_{ii\ell}(0). \tag{20}$$

The hidden variables introduced here are the analog of the memory variables used in viscoelastic wave simulation to describe dissipation caused by different relaxation processes (see Carcione, 1990, 1993). A similar approach, based on a time-domain permittivity function, was presented in Luebbers et al., (1990). They use an FDTD formulation to study the effects of water relaxation on the reflection coefficient at an air-water interface.

The wave equation

From equation (15), the conductivity terms on the right-hand side of equations (11) and (12) become

$$\sigma_{ii} * \frac{\partial E_m}{\partial t} = \sigma_{ii}^0 \left(E_m + \xi_{ii} \frac{\partial E_m}{\partial t} \right). \tag{21}$$

Substituting equations (19) and (21) into equations (11) and (12) gives

$$-\frac{\partial H_y}{\partial z} = \sigma_{e11}^\infty E_x + \epsilon_{e11}^\infty \frac{\partial E_x}{\partial t} + \epsilon_{11}^0 \sum_{\ell=1}^{L_1} e_{11\ell} + J_{sx}, \tag{22}$$

and

$$\frac{\partial H_y}{\partial x} = \sigma_{e33}^\infty E_z + \epsilon_{e33}^\infty \frac{\partial E_z}{\partial t} + \epsilon_{33}^0 \sum_{\ell=1}^{L_3} e_{33\ell} + J_{sz}, \tag{23}$$

where

$$\epsilon_{eii}^\infty = \epsilon_{ii}^\infty + \sigma_{ii}^0 \xi_{ii} \tag{24}$$

---

[1]In particular, given $f(t)$ and $g(t)$, the following relations hold: $f'\delta * g = f'(0)g$, and $f\delta' * g = f(0)g' - f'(0)g$.

and

$$\sigma_{eii}^{\infty} = \sigma_{ii}^{0} + \epsilon_{ii}^{0}\Phi_{ii} \tag{25}$$

are the effective optical permittivity and conductivity components, respectively.

The first two terms on the right-hand side of equations (22) and (23) correspond to the instantaneous response of the medium, as can be inferred from the relaxation functions (13) and (15). Note that the terms containing the conductivity relaxation time ξ_{ii} are in phase with the instantaneous polarization response. The third terms in each equation involve the relaxation processes through the hidden variables.

The wave equation is completed with the differential equations corresponding to the hidden variables. Time differentiation of equations (18) and the use of convolution properties yield

$$\frac{\partial e_{ii\ell}}{\partial t} = -\frac{1}{\tau_{ii\ell}}\left[e_{ii\ell} + \phi_{ii\ell}(0)E_i\right]. \tag{26}$$

Equations (10), (22), (23), and (26) give the electromagnetic response of a conducting anisotropic medium with dielectric relaxation behavior and out-of-phase conduction currents. These equations are the basis of the numerical algorithm, described in the last section, to obtain the field vector $[H_y, E_x, E_z, e_{ii\ell}]$, $i = 1, 3$, $\ell = 1, \ldots, L_i$. A similar set of equations, but without Debye relaxation mechanisms and out-of-phase currents, can be found in Carcione and Cavallini (1994).

As mentioned before, for completeness, Appendix A contains the wave equation corresponding to an arbitrary coordinate system. The use of this general equation is required when the Cartesian system where the problem is solved does not coincide with the principal system of the medium. In this way, the material properties can be modeled arbitrarily at any point of the model space.

When the medium is isotropic and there is no dielectric relaxation ($\lambda_{ii} = \tau_{ii}$) and out-of-phase conduction currents ($\xi_{ii} = 0$), it is $\phi_{ii\ell} = 0$ and $e_{11\ell} = e_{33\ell} = 0$; therefore equations (22) and (23) become

$$-\frac{\partial H_y}{\partial z} = \sigma E_x + \epsilon\frac{\partial E_x}{\partial t} + J_{sx}, \tag{27}$$

and

$$\frac{\partial H_y}{\partial x} = \sigma E_z + \epsilon\frac{\partial E_z}{\partial t} + J_{sz}, \tag{28}$$

where $\epsilon \equiv \epsilon^0 = \epsilon^{\infty}$ and $\sigma \equiv \sigma^0 = \sigma^{\infty}$ are the isotropic properties. Equations (10), (27), and (28) were used by Greenfield and Wu (1991) to model electromagnetic waves in coal seams.

PLANE-WAVE THEORY

A plane-wave analysis of the kinematic characteristics of electromagnetic uniform waves in absorbing anisotropic media can be found, for instance, in Born and Wolf (1975, 708). They assume a 3-D medium and frequency-independent dielectric and conductivity tensors. The use of relaxation functions to describe the material properties requires a more general analysis. This is presented in the next sections together with the calculation of the energy velocity (related to the ray surface) and the quality factor of the medium.

Dispersion relation for uniform waves

In the absence of magnetic moments, the time Fourier transform of equation (10) is

$$\nabla_2^{\top}\bullet\mathbf{E} = \iota\omega\mu H_y, \tag{29}$$

where $\mathbf{E} = [E_x, E_z]^{\top}$ and $\nabla_2 = [-\partial/\partial z, \partial/\partial x]^{\top}$, with the symbol $\top$ denoting transpose. Equations (11) and (12), in the absence of electric current sources, can be written in compact form as

$$\nabla_2 H_y = \frac{\partial\underset{\sim}{\sigma}}{\partial t}*\mathbf{E} + \frac{\partial\underset{\sim}{\epsilon}}{\partial t}*\frac{\partial\mathbf{E}}{\partial t}, \tag{30}$$

where, hereafter $\underset{\sim}{\epsilon} = \mathrm{diag}(\epsilon_{11}, \epsilon_{33})$ and $\underset{\sim}{\sigma} = \mathrm{diag}(\sigma_{11}, \sigma_{33})$. Using the convolution theorem, equation (30) becomes

$$\nabla_2 H_y = \iota\omega\left(\underset{\sim}{\tilde{\epsilon}} - \frac{\iota}{\omega}\underset{\sim}{\tilde{\sigma}}\right)\bullet\mathbf{E} = \iota\omega\left(\underset{\sim}{\epsilon}_e - \frac{\iota}{\omega}\underset{\sim}{\sigma}_e\right)\bullet\mathbf{E}, \tag{31}$$

where

$$\underset{\sim}{\epsilon}_e = \mathrm{Re}(\underset{\sim}{\tilde{\epsilon}}) + \frac{1}{\omega}\mathrm{Im}(\underset{\sim}{\tilde{\sigma}}) \tag{32}$$

and

$$\underset{\sim}{\sigma}_e = \mathrm{Re}(\underset{\sim}{\tilde{\sigma}}) - \omega\mathrm{Im}(\underset{\sim}{\tilde{\epsilon}}) \tag{33}$$

are the real effective permittivity and conductivity (diagonal) matrices, respectively, where the operators $\mathrm{Re}(\bullet)$ and $\mathrm{Im}(\bullet)$ take the real and imaginary part, respectively. The components of $\tilde{\underset{\sim}{\epsilon}}$ and $\tilde{\underset{\sim}{\sigma}}$ are

$$\tilde{\epsilon}_{ii} = \mathcal{F}\left[\frac{\partial\epsilon_{ii}}{\partial t}\right] = \frac{\epsilon_{ii}^0}{L_i}\sum_{\ell=1}^{L_i}\frac{1 + \iota\omega\lambda_{ii\ell}}{1 + \iota\omega\tau_{ii\ell}} \tag{34}$$

and

$$\tilde{\sigma}_{ii} = \mathcal{F}\left[\frac{\partial\sigma_{ii}}{\partial t}\right] = \sigma_{ii}^0(1 + \iota\omega\xi_{ii}), \tag{35}$$

with the operator $\mathcal{F}$ denoting time Fourier transform. Since $\lambda_{ii\ell} \leq \tau_{ii\ell}$ implies $\mathrm{Im}(\tilde{\epsilon}_{ii}) \leq 0$, and $\mathrm{Re}(\tilde{\sigma}_{ii}) \geq 0$, the two terms on the right-hand side of equation (33) have the same sign, and the wave process is always dissipative. The importance of the effective matrices is that their components are the quantities that are measured in laboratory experiments; ϵ_e produces a current out-of-phase with the electric field, while σ_e produces a current that varies in phase with the electric field. Note that the coefficients multiplying the electric field and the time derivative of the electric field in equations (22) and (23), correspond to the components of $\underset{\sim}{\sigma}_e^{\infty}$ and $\underset{\sim}{\epsilon}_e^{\infty}$, respectively.

Multiplying equation (31) from the left by $\nabla_2^{\top}\bullet\underset{\sim}{\beta}$, where

$$\underset{\sim}{\beta} = \left(\underset{\sim}{\epsilon}_e - \frac{\iota}{\omega}\underset{\sim}{\sigma}_e\right)^{-1} \tag{36}$$

is the (effective) dielectric impermeability matrix, and substituting equation (29), gives

$$\left(\nabla_2^{\top}\bullet\underset{\sim}{\beta}\bullet\nabla_2\right)H_y + \mu\omega^2 H_y = 0. \tag{37}$$

The magnetic field associated with a uniform TM plane wave has the form

$$\mathbf{H} = H_y\mathbf{e}_2, \qquad H_y \equiv H_0\exp\left[-\iota k\hat{\boldsymbol{\kappa}}^{\top}\bullet\mathbf{x}\right], \tag{38}$$

$$\mathbf{e}_2 \equiv [0, 1, 0]^{\top},$$

where $\mathbf{x} = [x, z]^\top$;

$$k = \kappa - \iota\alpha \tag{39}$$

is the complex wavenumber, where κ and α are the magnitudes of the real propagation and attenuation vectors, respectively; H_0 is a complex constant, and

$$\hat{\boldsymbol{\kappa}} = [\ell_x, \ell_z]^\top \tag{40}$$

defines the propagation (and attenuation) direction through the direction cosines ℓ_x and ℓ_z. Since for the plane wave equation (38) is

$$\nabla_2 \to -\iota\underline{\mathbf{K}}_2, \qquad \underline{\mathbf{K}}_2 = k[-\ell_z, \ell_x]^\top, \tag{41}$$

the substitution of equation (41) into equation (37) gives the dispersion relation

$$\beta_{33}\ell_x^2 + \beta_{11}\ell_z^2 - \mu\left(\frac{\omega}{k}\right)^2 = 0. \tag{42}$$

Kinematics of the wave propagation

The dispersion relation (42) defines the complex velocity

$$V \equiv \frac{\omega}{k} = \left(\frac{\beta_{33}\ell_x^2 + \beta_{11}\ell_z^2}{\mu}\right)^{1/2}. \tag{43}$$

The real attenuation and slowness vectors can be expressed in terms of the complex velocity as

$$\boldsymbol{\alpha} = -\omega\,\mathrm{Im}\left(\frac{1}{V}\right)\hat{\boldsymbol{\kappa}} \tag{44}$$

and

$$\mathbf{s} \equiv \frac{\kappa}{\omega}\hat{\boldsymbol{\kappa}} = \mathrm{Re}\left(\frac{1}{V}\right)\hat{\boldsymbol{\kappa}}, \tag{45}$$

while the phase velocity is, in magnitude, the reciprocal of the slowness and, in vector form, is given by

$$\mathbf{V}_p = \left[\mathrm{Re}\left(\frac{1}{V}\right)\right]^{-1}\hat{\boldsymbol{\kappa}}. \tag{46}$$

Similar equations were obtained by Carcione (1994) for shear viscoelastic plane waves in the symmetry plane of a monoclinic medium.

Umov–Poynting theorem, energy velocity and quality factor

The energy balance equation for time harmonic fields, in the absence of magnetic moments and electric currents, is (Booker, 1982; Magid, 1981)

$$\nabla \cdot \mathbf{P} - 2i\omega[(w_e)_{AV} - (w_m)_{AV}] + (p_d)_{AV} = 0, \tag{47}$$

where $\mathbf{P}$ is the complex Umov–Poynting vector defined as

$$\mathbf{P} = \tfrac{1}{2}(\mathbf{E} \times \mathbf{H}^*), \tag{48}$$

with the asterisk denoting complex conjugation and the symbol $\times$ indicating vector product. The real part of the Umov–Poynting vector gives the average power flow density over a cycle. The quantities

$$(w_e)_{AV} = \tfrac{1}{4}\,\mathrm{Re}\left[(\mathbf{E}^*)^\top \cdot \underline{\boldsymbol{\epsilon}}_e \cdot \mathbf{E}\right] \tag{49}$$

and

$$(w_m)_{AV} = \tfrac{1}{4}\,\mathrm{Re}\left[(\mathbf{H}^*)^\top \cdot \underline{\boldsymbol{\mu}} \cdot \mathbf{H}\right] \tag{50}$$

are the time-average electric and magnetic energy densities, and

$$(p_d)_{AV} = \tfrac{1}{2}\,\mathrm{Re}\left[(\mathbf{E}^*)^\top \cdot \underline{\boldsymbol{\sigma}}_e \cdot \mathbf{E}\right] \tag{51}$$

is the time-average dissipated power density. The identification of the energy and power densities in the energy balance equation is controversial when the wave process is dissipative [see, for instance, Caviglia and Morro (1992) 55]. Equation (47) is similar to an energy balance equation obtained in Carcione and Cavallini (1993) for inhomogeneous viscoelastic plane waves. The physical interpretation leading to equations (49) and (51) is that the dielectric relaxation contributes to the dissipation and the out-of-phase conduction current contributes to the stored electric energy. Mathematically, the first is in phase with the power dissipated by the conductivity properties, and the second is in phase with the stored electric energy.

For uniform plane waves of the form (38), the Poynting theorem (47) becomes

$$2\boldsymbol{\alpha}^\top \cdot \mathbf{P} + 2i\omega[(w_e)_{AV} - (w_m)_{AV}] - (p_d)_{AV} = 0. \tag{52}$$

The Umov–Poynting vector and energy densities for TM waves are calculated in Appendix B.

The energy velocity is the ratio between the average power flow $\mathrm{Re}(\mathbf{P})$ and the mean energy density $(w)_{AV} = (w_e + w_m)_{AV}$ (Chen, 1983). Hence,

$$\mathbf{V}_e = \frac{\mathrm{Re}(\mathbf{P})}{(w_e + w_m)_{AV}}. \tag{53}$$

Substitution of the Umov–Poynting vector (B-3) and the energy densities (B-4) and (B-7) into equation (53), and using the properties of complex numbers, give

$$\mathbf{V}_e = \frac{V_p}{\mu\,\mathrm{Re}(V)}\left[\ell_x\,\mathrm{Re}\left(\frac{\beta_{33}}{V}\right)\mathbf{e}_1 + \ell_z\,\mathrm{Re}\left(\frac{\beta_{11}}{V}\right)\mathbf{e}_3\right], \tag{54}$$

where V_p is the magnitude of the phase velocity defined in equation (46). The location of the energy defines the wavefront. Therefore, this is the locus of the tip of the energy velocity vector at unit propagation time.

The quality factor quantifies, somehow, energy dissipation in matter from the electric current standpoint. As stated in Harrington (1961, 28), the quality factor is defined as the magnitude of reactive current density to the magnitude of dissipative current density. In viscoelastodynamics, a common definition of quality factor is twice the ratio between the average potential energy density and the dissipated energy density. Accordingly, and using the acoustic-electromagnetic analogy (Carcione and Cavallini, 1995) the quality factor is defined here as twice the ratio between the average electric energy to the density of energy dissipated in one cycle:

$$Q = 2\omega\frac{(w_e)_{AV}}{(p_d)_{AV}}, \tag{55}$$

which from equations (B-7) and (B-8) becomes

$$Q = \frac{\mathrm{Re}(V^2)}{\mathrm{Im}(V^2)}. \tag{56}$$

It can be shown that, for isotropic low loss media, equation (56) reduces to the quality factor used by Turner and Siggins (1994).

The concept of quality factor can be considered as a generalization of the concept of Q in circuit theory. Good dielectrics have high Q values, and conductors have very low Q values.

SIMULATIONS

To illustrate the numerical solution algorithm, I consider the equations expressed in the principal system with one dielectric relaxation mechanism. Equations (10), (22), (23), and (26) can be written in compact matrix form as

$$\frac{\partial \mathbf{V}}{\partial t} = \underset{\sim}{\mathbf{A}}\mathbf{V} + \mathbf{S}, \tag{57}$$

where

$$\mathbf{V} = [H_y, E_x, E_z, e_{11}, e_{33}]^\top \tag{58}$$

is the unknown vector field, $\mathbf{S}$ is the source vector, and

$$\underset{\sim}{\mathbf{A}} = \begin{bmatrix} 0 & -\mu^{-1}\partial_z & \mu^{-1}\partial_x & 0 & 0 \\ -(\epsilon_{e11}^\infty)^{-1}\partial_z & -(\epsilon_{e11}^\infty)^{-1}\sigma_{e11}^\infty & 0 & -(\epsilon_{e11}^\infty)^{-1}\epsilon_{11}^0 & 0 \\ (\epsilon_{e33}^\infty)^{-1}\partial_x & 0 & -(\epsilon_{e33}^\infty)^{-1}\sigma_{e33}^\infty & 0 & -(\epsilon_{e33}^\infty)^{-1}\epsilon_{33}^0 \\ 0 & -\Phi_{11}\tau_{11}^{-1} & 0 & -\tau_{11}^{-1} & 0 \\ 0 & 0 & -\Phi_{33}\tau_{33}^{-1} & 0 & -\tau_{33}^{-1} \end{bmatrix} \tag{59}$$

where ∂_x and ∂_z denote spatial derivatives.

Equation (57) is solved with a direct grid method that computes the spatial derivatives by using the Fourier pseudospectral method (e.g., Canuto et al., 1988) and propagates the solution in time with a fourth-order Runge–Kutta algorithm.

However, when there is a Debye peak whose central frequency is much larger than the dominant frequency of the source, the equations become stiff (Jain, 1984). In this case, a partition (or splitting) time integrator algorithm is used. The stiff part is solved analytically and the nonstiff part is solved by the Runge–Kutta algorithm (see Appendix C), whose stability region can be found in Canuto et al. (1988, 109). The modeling significantly improves with this approach. However, a better technique in terms of numerical stability, such as an implicit algorithm, should improve its performance further.

A modeling software package, Georadar Electromagnetic Modeling and Simulation (GEMS), was developed and designes the geological model, provides the kinematic and dynamic properties of each medium, and generates the radargrams for a variety of antenna configurations.

Finely stratified sand

The first simulation considers a homogeneous, finely laminated, sandy medium; i.e., the wave characteristics along the vertical and horizontal directions differ. The material properties are the following: $\epsilon_{11}^\infty = 15\epsilon_0$, $\epsilon_{33}^\infty = 10\epsilon_0$, $\sigma_{11}^0 = 10^{-3}$ S/m and $\sigma_{33}^0 = 3 \times 10^{-3}$ S/m; there is a Debye mechanism centered at 1 GHz with relaxation times $\tau_{11} = 0.163$ ns, $\lambda_{11} = 0.155$ ns, $\tau_{33} = 0.257$ ns and $\lambda_{33} = 0.098$ ns; there are no
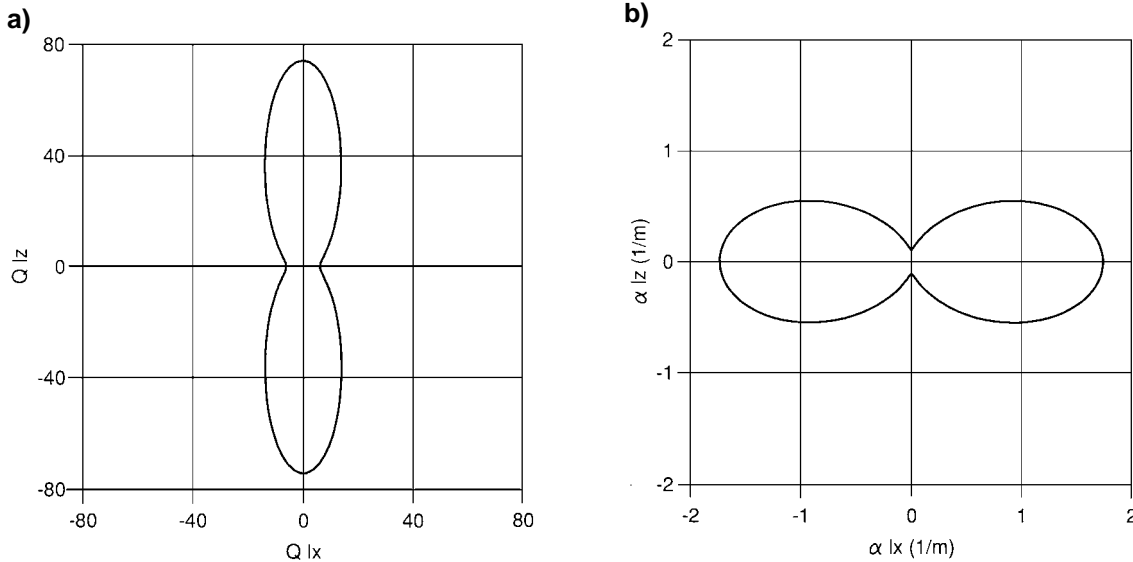

FIG. 1. (a) Quality factor, (b) attenuation, (c) energy velocity, and (d) snapshot corresponding to an anisotropic conducting medium with a Debye relaxation mechanism centered at 1 GHz. The curves are given at a frequency of 200 MHz, that is also the source dominant frequency. Figure 1e and 1f correspond to the same material, but without the Debye relaxation peak. In this case, the medium is practically lossless.

out-of-phase conduction currents ($\xi_{ii} = 0$); the magnetic permeability μ has been taken equal to that of vacuum ($\mu_0 = 4\pi 10^{-7}$ Hm^{-1}) and $\epsilon_0 = 8.85 \ 10^{-12}$ Fm^{-1}. Figure 1 shows the quality factor (a), the attenuation (b) and the energy velocity (c) at a frequency of 200 MHz. Note that the behavior along the x-direction is determined by (33) components, while (11) components define the wave characteristics along the z-direction (Born and Wolf, 1975, 675). The dissipation is mainly caused by the Debye relaxation, which yields a Q factor of less than 10 along the horizontal axis (the vertical and horizontal quality factors caused by the conductivity are approximately 160 and 40, respectively). Figure 1e represents the energy velocity without the Debye dissipation mechanism. The main difference with Figure 1c is the value of the horizontal velocity,

because of dispersion caused by the high dissipation. This effect transforms the medium from negative uniaxial (Figure 1e) into positive uniaxial (Figure 1c) [see Born and Wolf (1975, 680) for the definition of positive and negative uniaxial media].

The numerical mesh used to solve equation (57) has $N_X = N_Z = 135$ grid points per side, with a uniform grid spacing of $D_X = D_Z = 7.5$ cm. The field is initiated by a magnetic current, [a line source normal to the (x, z)-plane] with a central frequency of 200 MHz, and is propagated with a time step of 0.05 ns. Figures 1d and 1f represent the snapshots of the magnetic field at 50 ns, with and without the Debye relaxation, respectively. As can be seen, the results of the simulations are in agreement with the wave characteristics predicted by the plane-wave analysis.
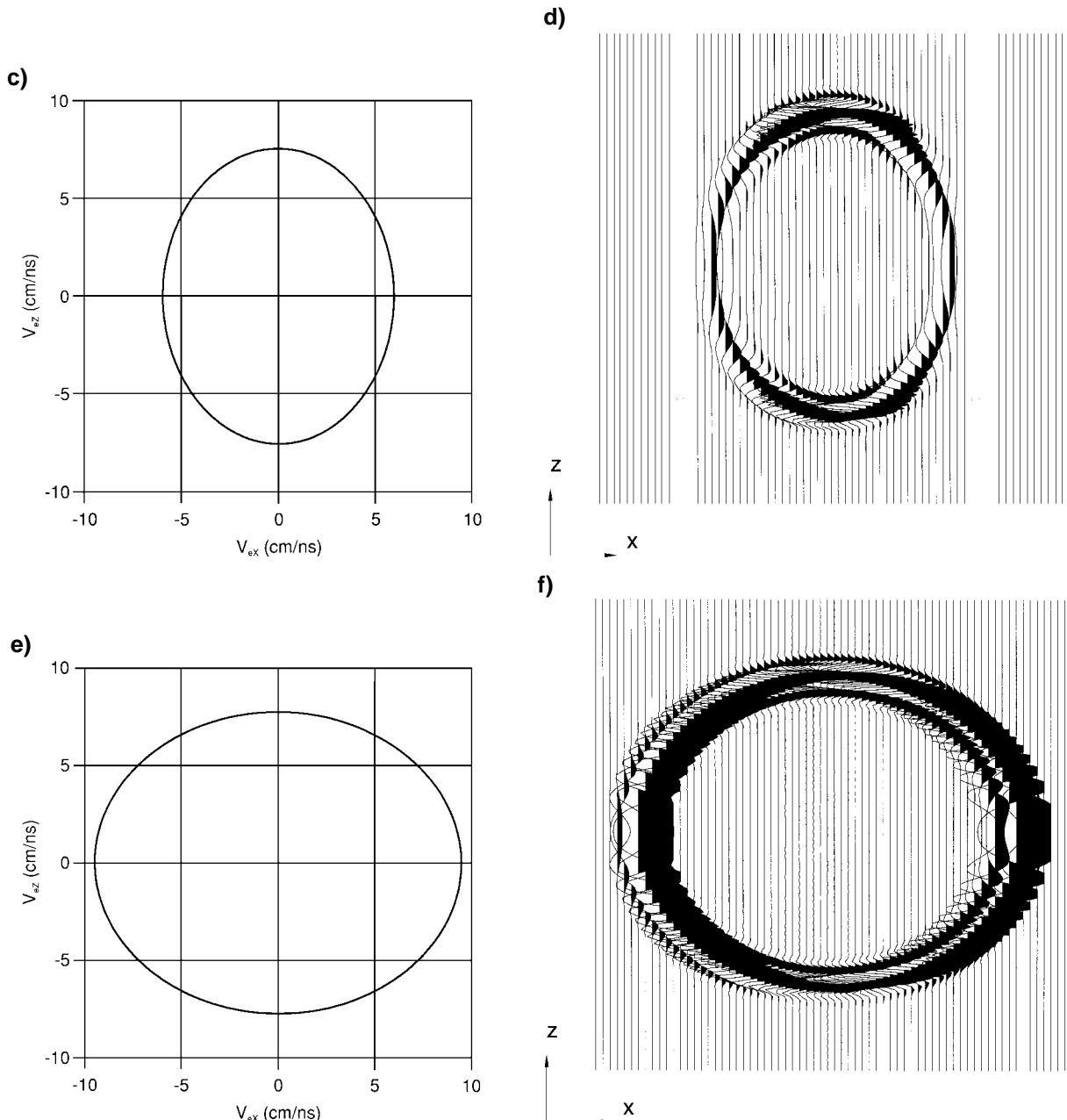

FIG. 1. (Continued.)

A transient analytical solution, without dielectric relaxation, was obtained by Carcione and Cavallini (1995). Since the Green's function is given in the frequency-domain, the solution can be extended easily to include Debye relaxation mechanisms. Figure 2 compares numerical and analytical solutions at the location $(x, z) = (3, 2)$ m relative to the source position. The agreement between solutions is virtually perfect.

Dense nonaqueous phase liquids

The second simulation is based on a GPR survey of dense nonaqueous phase liquids (DNAPLs) carried out by Brewster and Annan (1994). DNAPLs are common nonwetting groundwater contaminants, denser than water, that have a very low dielectric permittivity compared to water. This characteristic makes them a potential target for the radar. The geological model is represented in Figure 3, where the DNAPL pools are indicated by black areas and the lower interface is the top of a clay aquitard. The material properties are given in Table 1. The coefficient of anisotropy in the electrical conductivity $(\sigma_{33}^0/\sigma_{11}^0)^{1/2}$ is 1.7 for the sand and 1.4 for shale. They are in the range given in Negi and Saraf (1989) for typical geological formations. The anisotropy in the dielectric properties results from the assumption that the rocks are saturated with fluids and have a fine laminated structure. The sand is partially saturated with water, and has horizontal and vertical velocities of 7 and 6 cm/ns, respectively. A Debye relaxation at 1 GHz, together with the dc conductivity, yields horizontal and vertical quality factors of approximately 40 and 120, respectively. On the other

hand, the pools are isotropic (the velocity is 8 cm/ns) with an extremely low conductivity, and the clay is highly conductive.

The following numerical experiment simulates a stacked radargram obtained from the processing of a series of common "shots" gathers. The number of grid points, grid spacing, and source central frequency are the same as for the preceding example. The source is a horizontal electrical current (J_{sx}) plane wave at the air-sand interface (vertical gridpoint 20 of the numerical mesh). Figures 4a and 4b represent the radargrams for the magnetic field, corresponding to the anisotropic and isotropic cases, respectively. The isotropic case is obtained by assuming that (11) components are equal to (33) components. In the interval between 0 and 15 ns, the signal is a combination of the direct air wave and the direct ground wave, and the event between 100 and 125 ns is the reflection of the top of the clay aquitard. Below this event, the signals are probably multiple reflections originated between the pools and the surface, since the clay is highly conductive and acts as a barrier for the electromagnetic waves. Within the sand aquifer, the various reflectors correspond to the DNAPL pools and can be easily identified in Figure 4a. Only the pools between 1 and 2 m depth might be taken as one, since the signal cannot resolve the distance between them. The lower pool can hardly be seen in Figure 4b, and the others are attenuated and have a different arrival time with respect to Figure 4a. This is because ϵ_{11} determines the phase velocity along the vertical direction. Obviously, the spatial extent of the reflectors does not represent the real dimensions of the pools, since part of the energy is diffracted at their edges. Note that the presence of the pools
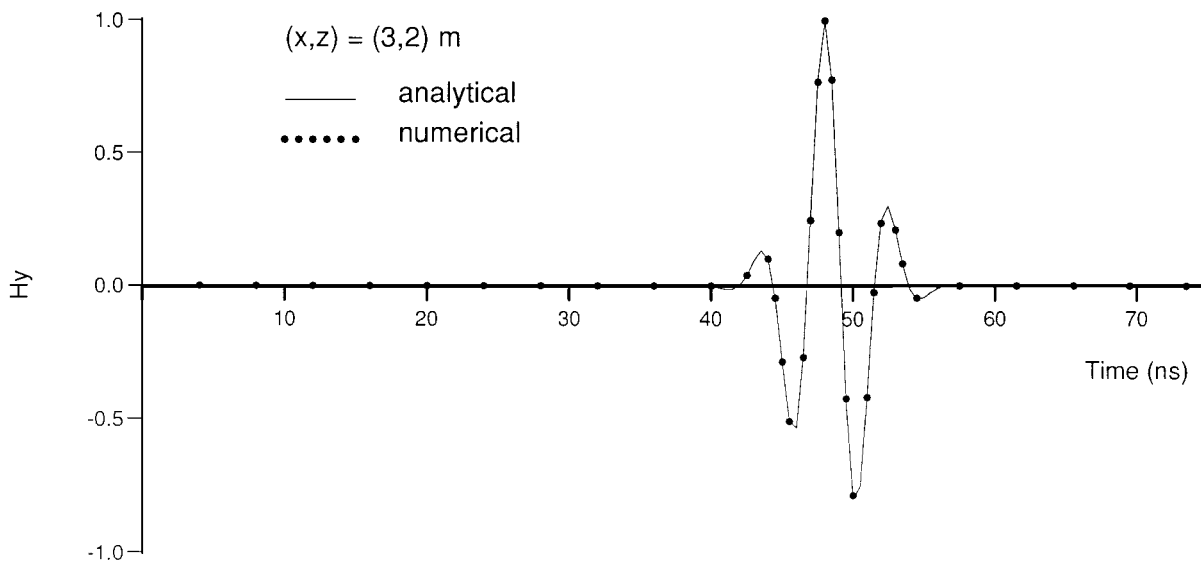

FIG. 2. Comparison between numerical and analytical solutions. The source central frequency is 200 MHz and the receiver location is $(x, z) = (3, 2)$ m relative to the source position.

Table 1. Material properties.

Medium	$\epsilon_{11}^\infty (\epsilon_0)$	$\epsilon_{33}^\infty (\epsilon_0)$	σ_{11}^0 (S/m)	σ_{33}^0 (S/m)	τ_{11} (ns)	λ_{11} (ns)	τ_{33} (ns)	λ_{33} (ns)
Air	1	1	0	0	——	——	——	——
Sand	25	20	10^{-3}	3×10^{-3}	0.161	0.156	0.165	0.153
DNAPL	13.4	13.4	10^{-6}	10^{-6}	——	——	——	——
Clay	8	5	0.3	0.6	0.160	0.158	0.161	0.157

$\epsilon_0 = 8.85 \ 10^{-12}$ F m^{-1}; $\mu = \mu_0 = 4\pi \ 10^{-7}$ H m^{-1}.

and the high velocity of the DNAPL produce a fading and a pull-up of the aquitard reflector.

On the other hand, if one assumes that (33) components are equal to (11) components, the corresponding radargram will be similar to that represented in Figure 4a, since the plane-wave source simulates a zero-offset survey. However, consider a "common-shot" experiment, with the source and the receivers located at the air-sand interface. The comparison between the anisotropic (a) and the isotropic (b) radargrams (magnetic field) can be appreciated in Figure 5. They almost coincide for near-offsets, but are different for offsets beyond one meter approximately: the anisotropic dielectric and conductivity properties have considerably altered the amplitude and arrival time of the first reflection event.

CONCLUSIONS

Modeling radio waves in a realistic medium involves several aspects. In the first place, the wave equation should permit the proper simulation of the complete wave field, i.e., the reflections (single and multiples), the refractions, and the diffracted waves. Moreover, in the case of soils and rocks, the petrophysical and lithological properties play an important role. In particular, fine layering (anisotropy), ionic conductivity in partially saturated porous media, and dielectric relaxation processes, have a significant influence on the attributes (amplitude and arrival time) of the radar pulses.

The proposed modeling technique uses a relaxation tensor formulation of the dielectric and conductivity properties, that accounts for anisotropic properties and the various dissipation mechanisms of the radio frequency band. In particular, the Debye relaxations require the introduction of hidden variables that are solved together with the electric and magnetic fields. A direct grid method solver, based on the Fourier differential operator, allows the modeling of the complete wavefield. The stiffness of the differential equations (caused by the relaxation processes) is handled with a time-splitting integration algorithm.

A plane-wave analysis, based on uniform plane waves, gives the expressions of measurable quantities, like the quality factor and the energy velocity, as a function of the frequency and the propagation direction. The concept of an effective dielectric impermeability matrix is introduced to properly define the electric and dissipated energy densities. The theory and the modeling applied to a finely laminated sandy medium shows how the material transforms from negative uniaxial to positive uniaxial when a Debye peak (with a high Q factor) is introduced. For instance, this may represent the difference between a dry and a water saturated porous material, since the latter is affected by the bound water relaxation mechanism. Another application of the modeling is the computation of the electromagnetic response (a multichannel array survey) of dense nonaqueous phase liquids (DNAPL) that contaminate a sand aquifer. The reflectors corresponding to the DNAPL pools can be seen clearly because of the permittivity contrast between the sand and the contaminant. In this way, the modeling predicts the potential georadar visibility of contaminants in
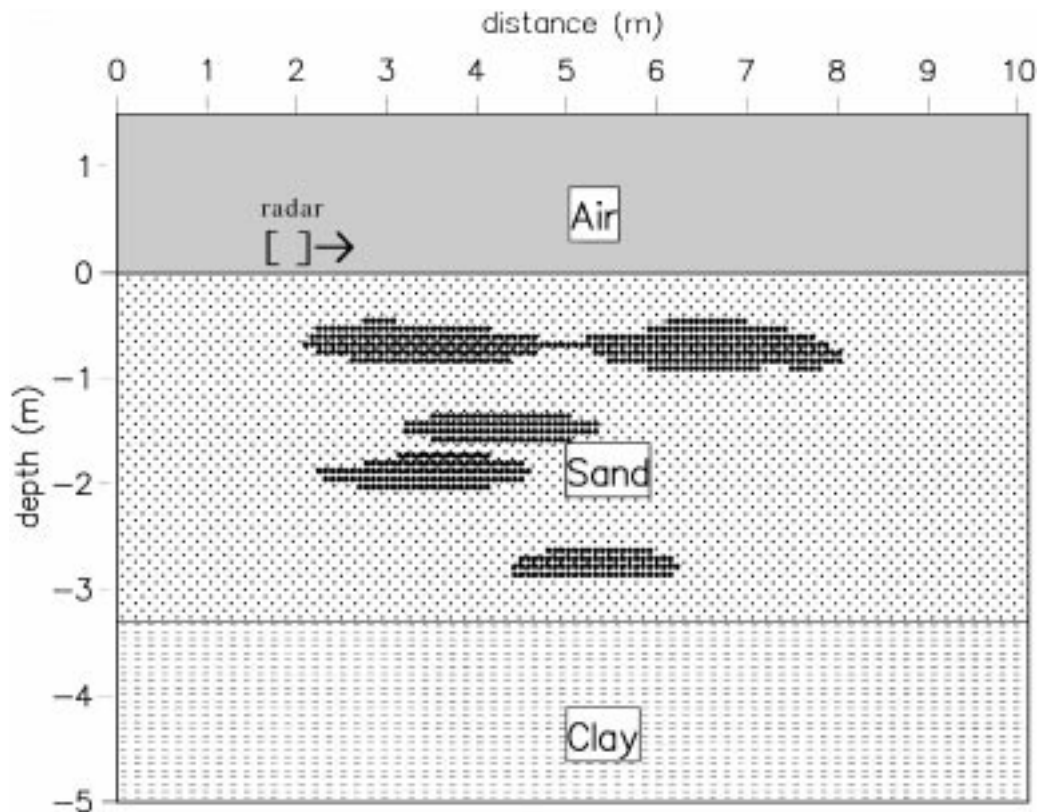

FIG. 3. Geological model representing DNAPL contamination pools (black areas) in a sand aquifer. The sand is anisotropic (finely laminated) and has a Debye relaxation at 1 GHZ. On the other hand, the DNAPL is isotropic and lossless. The material properties are given in Table 1.
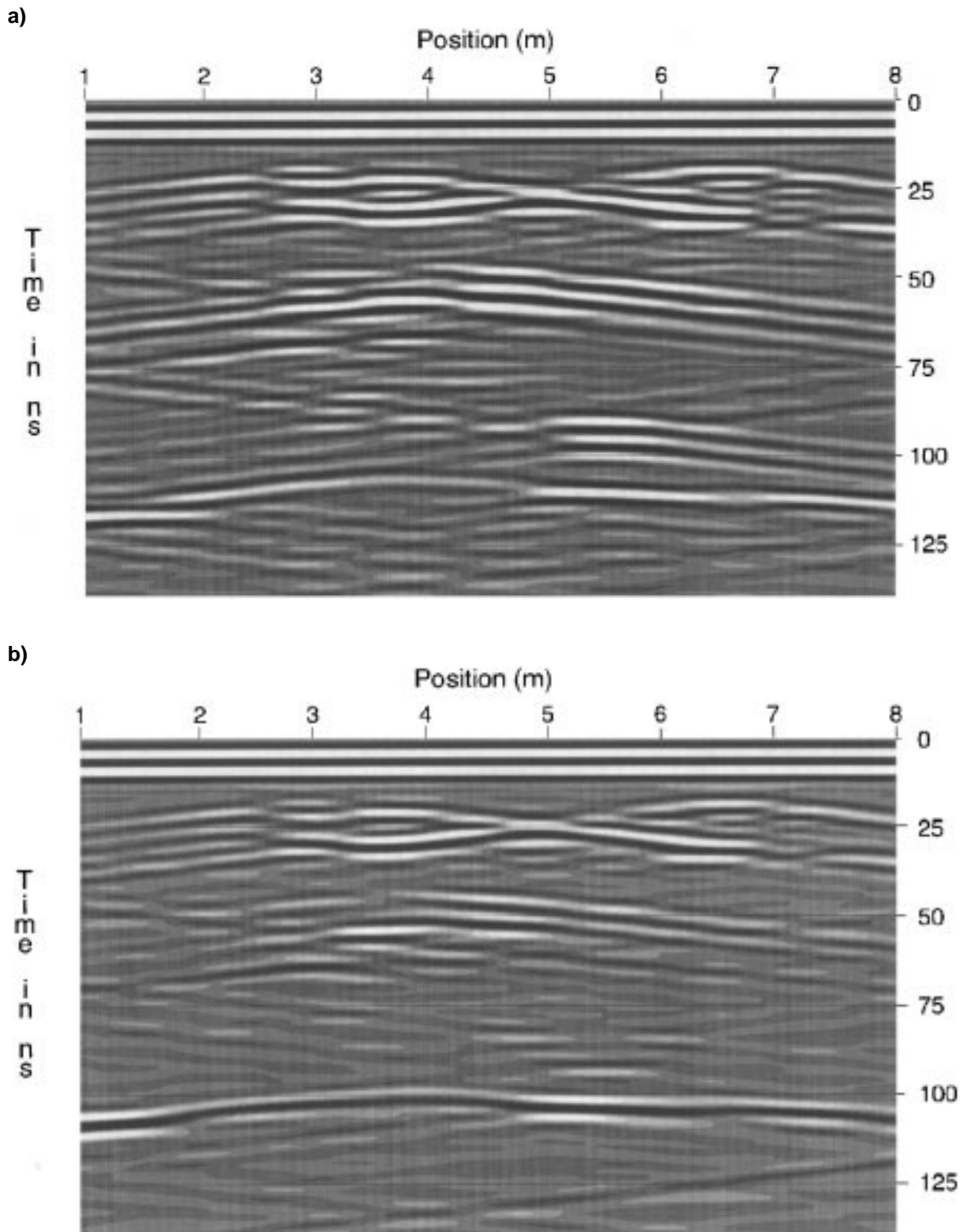
a)

b)

FIG. 4. Plane-wave synthetic radargrams for the magnetic field, corresponding to the (a) anisotropic and (b) isotropic cases. The latter is obtained by assuming that (11) components are equal to (33) components. The source is a horizontal electric current (plane-wave) at the air-sand interface (see Figure 2), and has a dominant frequency of 200 MHz.
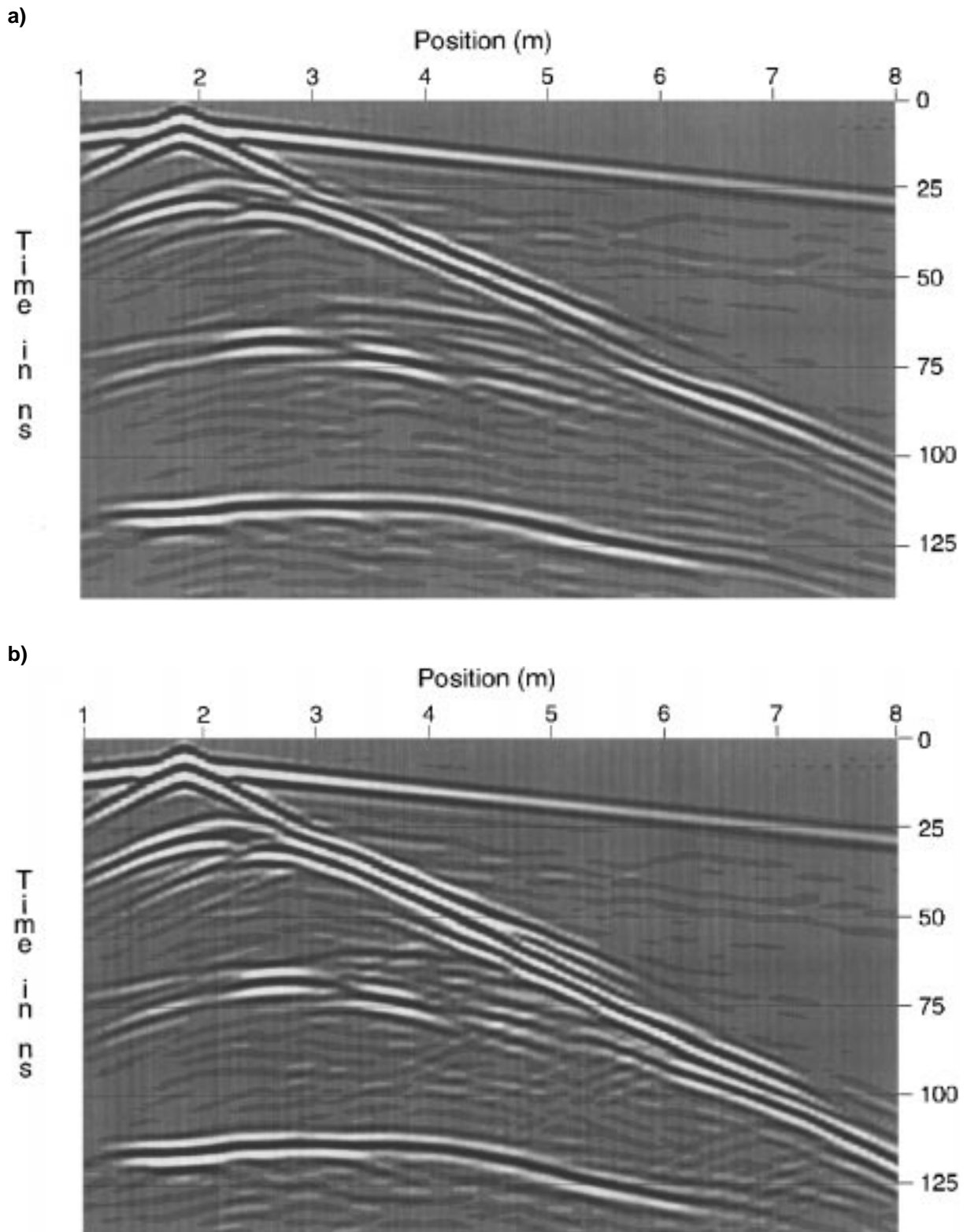
a)

b)

FIG. 5. "Common shot" synthetic radargrams for the magnetic field, corresponding to (a) anisotropic and (b) isotropic cases. The latter is obtained by assuming that (33) components are equal to (11) components. The source is a horizontal electric current applied at a point of the air-sand interface, and has a dominant frequency of 200 MHz.

porous soils. Moreover, comparison between the anisotropic and isotropic radargrams indicate the importance of considering the anisotropy of the permittivity and conductivity properties. Future research includes a detailed simulation of the antenna radiation pattern and extension of the theory and the modeling technique to the 3-D case.

REFERENCES

Bevan, B. W., 1991, The search for graves: Geophysics, **56**, 1310–1319.
Booker, H. G., 1982, Energy in electromagnetism: IEEE Electromagnetics wave series 13.
Born, M., and Wolf, E., 1975, Principles of optics: Oxford, Pergamon Press.
Brewster, M. L., and Annan, P., 1994, Ground-penetrating radar monitoring of a controlled DNAPL release: 200 MHz radar: Geophysics, **59**, 1211–1221.
Canuto, C., Hussaini, M. Y., Quarteroni, A., and Zang, T. A., 1988, Spectral methods in fluid dynamics: Springer-Verlag.
Carcione, J. M., 1990, Wave propagation in anisotropic linear viscoelastic media: Theory and simulated wavefields: Geophys. J. Internat., **101**, 739–750. Erratum: 1992, **111**, 191.
—— 1993, Seismic modeling in viscoelastic media: Geophysics, **58**, 110–120.
—— 1994, Wavefronts in dissipative anisotropic media: Geophysics, **59**, 644–657.
Carcione, J. M., and Cavallini, F., 1993, Energy balance and fundamental relations in anisotropic viscoelastic media: Wave Motion, **18**, 11–20.
—— 1994, Modeling transverse electromagnetic waves in conducting anisotropic media by a spectral time-domain technique, *in* Terzuoli, A., Ed., 10th annual review of progress in applied computational electromagnetics, Vol. II, 586–593.
—— 1995, On the acoustic-electromagnetic analogy: Wave Motion, **21**, 149–162.
Carcione, J. M., and Quiroga-Goode, G., 1994, Some aspects of the physics and numerical modeling of Biot compressional waves: J. Comput. Acoust, **4**, 261–280.

Casula, G. and Carcione, J. M., 1992, Generalized mechanical model analogies of linear viscoelastic behavior: Boll. Geofis. Teor. Appl., **34**, 235–256.
Caviglia, G., and Morro, A., 1992, Inhomogeneous waves in solids and fluid: World Scientific Co.
Chen, H. C., 1983, Theory of electromagnetic fields: Mc-Graw Hill Book Co.
Chew, W. C., 1990, Waves and fields in inhomogeneous media: Van Nostrand Reinhold Co.
Davis, J. L., and Annan, P., 1989, Ground-penetrating radar for high-resolution mapping of soil and rock stratigraphy: Geophys. Prosp., **37**, 531–551.
Fisher, E., McMechan, G. A., and Annan, P., 1992, Acquisition and processing of wide-aperture ground-penetrating radar data: Geophysics, **57**, 495–504.
Goodman, D., 1994, Ground-penetrating radar simulation in engineering and archeology: Geophysics, **59**, 224–232.
Greenfield, R. J., and Wu, T., 1991, Electromagnetic wave propagation in disrupted coal seams: Geophysics, **56**, 1571–1577.
Harrington, R. F., 1961, Time-harmonic electromagnetic fields, Mc-Graw Hill Book Co.
Hasted, J. B., 1973, Aqueous dielectrics: Chapman and Hall.
Imai, T., Sakayama, T., and Kanemori, T., 1987, Use of ground-penetrating radar and resistivity surveys for archeological investigations: Geophysics, **52**, 137–150.
Jain, M. K., 1984, Numerical solutions of partial differential equations: Wiley Eastern Ltd.
King, R. W. P., and Smith, G. S., 1981, Antennas in matter: M. I. T. Press.
Lau, C. L., Scullion, T., and Chan, P., 1992, Using ground-penetrating radar technology for pavement evaluations in Texas, USA: Finland Geol. Sur., 4th International Conferenec on Ground Penetrating Radar, special paper /bf 16, 277–283.
Luebbers, R., Hunsberger, F. P., Kunz, K. S., Standler, R. B., and Schneider, M., 1990, A frequency-dependent finite-difference time-domain formulation for dispersive materials: IEEE Trans. Electromagnetic Compat., **32**, 222–227.
Magid, L. M., 1981, Electromagnetic fields, energy and waves: Robert E. Krieger Co.
Negi, J. G., and Saraf, P. D., 1989, Anisotropy in geoelectromagnetism: Elsevier Co.
Turner, G., and Siggins, A. F., 1994, Constant Q attenuation of subsurface radar pulses: Geophysics, **59**, 1192–1200.
Ursin, B., 1983, Review of elastic and electromagnetic wave propagation in horizontally layered media: Geophysics, **48**, 1063–1081.
Witterholt, E. J., and Kretzschmar, J. L., 1984, Mapping of a steam flood with MHz EM waves: 54th Ann. Internat. Mtg. Soc. Expl. Geophys., Expanded Abstracts, 719–721.

APPENDIX A

ELECTROMAGNETIC EQUATIONS IN AN ARBITRARY COORDINATE SYSTEM

In general media, each point of the model space has arbitrary anisotropic properties and the propagation of TM waves requires the introduction of (13) components in addition to (11) and (33) components.

Denote $\bar{\epsilon}_{ij}$ the permittivity components in the Cartesian system where the problem is solved. Then, they can be expressed in terms of the principal components as

$$
\begin{bmatrix} \bar{\epsilon}_{11} & \bar{\epsilon}_{13} \\ \bar{\epsilon}_{13} & \bar{\epsilon}_{33} \end{bmatrix} = \begin{bmatrix} \cos\theta_\epsilon & -\sin\theta_\epsilon \\ \sin\theta_\epsilon & \cos\theta_\epsilon \end{bmatrix} \cdot \begin{bmatrix} \epsilon_{11} & 0 \\ 0 & \epsilon_{33} \end{bmatrix} \cdot \begin{bmatrix} \cos\theta_\epsilon & \sin\theta_\epsilon \\ -\sin\theta_\epsilon & \cos\theta_\epsilon \end{bmatrix}, \quad \text{(A-1)}
$$

where θ_ϵ is the angle of rotation and the dot denotes the ordinary matrix product. A similar equation can be written for the conductivity components $\bar{\sigma}_{ij}$ and the rotation angle θ_σ.

Then, it can be shown that the equations corresponding to equations (22) and (23) are

$$
\begin{aligned}
-\frac{\partial H_y}{\partial z} &= \left(\bar{\sigma}_{11}^0 + \epsilon_{11}^0 \Phi_{11} \cos^2\theta_\epsilon + \epsilon_{33}^0 \Phi_{33} \sin^2\theta_\epsilon \right) E_x \\
&+ \left(\bar{\epsilon}_{11}^\infty + \sigma_{11}^0 \xi_{11} \cos^2\theta_\sigma + \sigma_{33}^0 \xi_{33} \sin^2\theta_\sigma \right) \frac{\partial E_x}{\partial t} \\
&+ \left[\bar{\sigma}_{13}^0 + \frac{1}{2}\sin(2\theta_\epsilon)\left(\epsilon_{11}^0\Phi_{11} - \epsilon_{33}^0\Phi_{33} \right) \right] E_z \\
&+ \left[\bar{\epsilon}_{13}^\infty + \frac{1}{2}\sin(2\theta_\sigma)\left(\sigma_{11}^0\xi_{11} - \sigma_{33}^0\xi_{33} \right) \right] \frac{\partial E_z}{\partial t} \\
&+ \epsilon_{11}^0 \sum_{\ell=1}^{L_1} \left[\cos^2(\theta_\epsilon)e_{11\ell}^{(x)} + \frac{1}{2}\sin(2\theta_\epsilon)e_{11\ell}^{(z)} \right] \\
&+ \epsilon_{33}^0 \sum_{\ell=1}^{L_3} \left[\sin^2(\theta_\epsilon)e_{33\ell}^{(x)} - \frac{1}{2}\sin(2\theta_\epsilon)e_{33\ell}^{(z)} \right] \\
&+ J_{sx}, \quad \text{(A-2)}
\end{aligned}
$$

$$\frac{\partial H_y}{\partial x} = \left[\tilde{\sigma}_{13}^0 + \frac{1}{2} \sin(2\theta_\epsilon)(\epsilon_{11}^0 \Phi_{11} - \epsilon_{33}^0 \Phi_{33}) \right] E_x$$

$$+ \left[\tilde{\epsilon}_{13}^\infty + \frac{1}{2} \sin(2\theta_\sigma)(\sigma_{11}^0 \xi_{11} - \sigma_{33}^0 \xi_{33}) \right] \frac{\partial E_x}{\partial t}$$

$$+ (\tilde{\sigma}_{33}^0 + \epsilon_{33}^0 \Phi_{33} \cos^2 \theta_\epsilon + \epsilon_{11}^0 \Phi_{11} \sin^2 \theta_\epsilon) E_z$$

$$+ (\tilde{\epsilon}_{33}^\infty + \sigma_{11}^0 \xi_{11} \sin^2 \theta_\sigma + \sigma_{33}^0 \xi_{33} \cos^2 \theta_\sigma) \frac{\partial E_z}{\partial t}$$

$$+ \epsilon_{33}^0 \sum_{\ell=1}^{L_3} \left[\cos^2(\theta_\epsilon) e_{33\ell}^{(z)} - \frac{1}{2} \sin(2\theta_\epsilon) e_{33\ell}^{(x)} \right]$$

$$+ \epsilon_{11}^0 \sum_{\ell=1}^{L_1} \left[\sin^2 \theta_\epsilon e_{11\ell}^{(z)} + \frac{1}{2} \sin(2\theta_\epsilon) e_{11\ell}^{(x)} \right] + J_{sz},$$

$$(A\text{-}3)$$

where new hidden variables $e_{11\ell}^{(z)}$ and $e_{33\ell}^{(x)}$ were introduced. The new set of hidden variables is defined by $e_{ii\ell}^{(m)} = -\phi_{ii\ell} * E_m / \tau_{ii\ell}$, where $m = 1(x)$ or $3(z)$, and the corresponding differential equation is

$$\frac{\partial e_{ii\ell}^{(m)}}{\partial t} = -\frac{1}{\tau_{ii\ell}} \left[e_{ii\ell}^{(m)} + \phi_{ii\ell}(0) E_m \right]. \qquad (A\text{-}4)$$

APPENDIX B

UMOV–POYNTING VECTOR AND ENERGY DENSITIES

In the 2-D TM notation, the Umov–Poynting vector (48) takes the following form

$$\mathbf{P} = \frac{1}{2} \begin{bmatrix} -E_z \\ E_x \end{bmatrix} H_y^*. \qquad (B\text{-}1)$$

From equations (31) and (41), and substituting the impermeability matrix (36), the electric field can be written as

$$\mathbf{E} = -\frac{H_y}{\omega} (\underset{\sim}{\beta} \cdot \mathbf{K_2}). \qquad (B\text{-}2)$$

By substituting (B-2) into (B-1), the mean power flow density becomes

$$\Re(\mathbf{P}) = \frac{1}{2} |H_0|^2 \exp(-2\alpha^\top \cdot \mathbf{x})$$

$$\times \Re \left[\frac{1}{V} (\beta_{33} \ell_x \mathbf{e}_1 + \beta_{11} \ell_z \mathbf{e}_3) \right], \quad (B\text{-}3)$$

where equations (38), (41), and (42) have been used.

From equations (50) and (38), the TM magnetic energy density is

$$(w_m)_{AV} = \frac{1}{4} \mu |H_0|^2 \exp(-2\alpha^\top \cdot \mathbf{x}). \qquad (B\text{-}4)$$

On the other hand, from equations (49) and (B-2), the electric energy density is

$$(w_e)_{AV} = \frac{1}{4} \frac{|H_0|^2}{\omega^2} \exp(-2\alpha^\top \cdot \mathbf{x})$$

$$\times \Re[(\mathbf{K_2}^*)^\top \cdot \underset{\sim}{\beta}^* \cdot \underset{\sim}{\epsilon}_e \cdot \underset{\sim}{\beta} \cdot \mathbf{K_2}], \quad (B\text{-}5)$$

where the fact that $\underset{\sim}{\beta}$ is a symmetric matrix has been used. Taking into account that $\underset{\sim}{\epsilon}_e = \Re(\underset{\sim}{\beta}^{-1})$, it is easy to show that $\underset{\sim}{\beta}^* \cdot \underset{\sim}{\epsilon}_e \cdot \underset{\sim}{\beta} = \Re(\underset{\sim}{\beta})$. Then,

$$(w_e)_{AV} = \frac{1}{4} \frac{|H_0|^2}{\omega^2} \exp(-2\alpha^\top \cdot \mathbf{x}) \Re[(\mathbf{K_2}^*)^\top \cdot \underset{\sim}{\beta} \cdot \mathbf{K_2}],$$

$$(B\text{-}6)$$

or, using equations (41) and (42),

$$(w_e)_{AV} = \frac{1}{4} \mu |H_0|^2 \exp(-2\underset{\sim}{\alpha}^\top \cdot \mathbf{x}) \frac{\Re(V^2)}{|V|^2}. \qquad (B\text{-}7)$$

Following the same steps used to obtain the electric energy density, and noting that $\underset{\sim}{\sigma}_e = -\omega \text{Im}(\underset{\sim}{\beta}^{-1})$ and $\underset{\sim}{\beta}^* \cdot \underset{\sim}{\sigma}_e \cdot \underset{\sim}{\beta} = \omega \text{Im}(\underset{\sim}{\beta})$, the dissipated power density is

$$(p_d)_{AV} = \frac{1}{2} \mu \omega |H_0|^2 \exp(-2\underset{\sim}{\alpha}^\top \cdot \mathbf{x}) \frac{\text{Im}(V^2)}{|V|^2}. \qquad (B\text{-}8)$$

APPENDIX C

TIME INTEGRATION FOR STIFF ELECTROMAGNETIC EQUATIONS

Assume an electromagnetic wave traveling in the x-direction with the magnetic and electric fields polarized in the y- and z-directions, respectively. When using the Fourier pseudospectral method, the wavenumbers κ supported by the numerical mesh span from zero to the Nyquist wavenumber π/D_X, where D_X is the grid spacing. In the wavenumber domain, the eigenvalues $\gamma = i\omega$ (ω complex) of matrix $\mathbf{A}$ satisfy the characteristic equation $\det(\underset{\sim}{\mathbf{A}} - \gamma \mathbf{I}) = 0$, or

$$\gamma \left[\left(\gamma + \frac{\sigma_e^\infty}{\epsilon_e^\infty} \right) \left(\gamma + \frac{1}{\tau} \right) - \frac{\Phi \epsilon^0}{\tau \epsilon_e^\infty} \right] + \left(\gamma + \frac{1}{\tau} \right) \frac{\kappa^2}{\mu \epsilon_e^\infty} = 0,$$

$$(C\text{-}1)$$

where $\sigma_e^\infty = \sigma^0 + \epsilon^0 \Phi$ and $\epsilon_e^\infty = \epsilon^\infty + \sigma^0 \xi$. When $\lambda = \tau$ and $\sigma_e^\infty = 0$, $\gamma = \pm \imath V_p \kappa$, where $V_p = 1/\sqrt{\epsilon_e^\infty \mu}$ is the phase velocity.

In this case, the eigenvalues lie in the imaginary axis. On the other hand, the general solution of equation (C-1) gives a static mode corresponding to a real and negative eigenvalue γ_s, and two propagating modes lying close to the imaginary axis, corresponding to the other eigenvalues. When the central frequency of a Debye peak is much larger than the dominant frequency of the source, $\gamma_s \approx -1/\lambda$, and its magnitude is much larger than the eigenvalues corresponding to the propagating modes. To have numerical stability, the domain of convergence of the time integration scheme should include the static eigenvalue. For instance, an explicit fourth-order Runge-Kutta method requires $dt\lambda_s > -2.78$, implying a very small time step dt. Then, the method is restricted by numerical stability rather than by accuracy. The presence of this large eigenvalue, together with small eigenvalues, indicates that the problem is *stiff* (Jain, 1984, 72).

The system of electromagnetic equations can be partitioned into two sets of differential equations, one stiff and the other

nonstiff. Consider for simplicity of equation (57), corresponding to (11) components. The stiff part is

$$\frac{\partial E_x}{\partial t} = -\frac{\epsilon_{11}^0}{\epsilon_{e11}^\infty} e_{11}, \tag{C-2}$$

$$\frac{\partial e_{11}}{\partial t} = -\frac{1}{\tau_{11}} \left[e_{11} + \Phi_{11} E_x \right]. \tag{C-3}$$

Now, assume that the solution at time ndt is E_x^n, e_{11}^n and $\partial e_{11}^n/\partial t = -(e_{11}^n + \Phi_{11} E_x^n)/\tau_{11}$. The solution at an intermediate time, labeled by an asterisk, can be obtained in analytical form. It yields

$$e_{11}^* = A \exp(\lambda_1 t) + B \exp(\lambda_2 t), \tag{C-4}$$

$$E_x^* = E_x^n - \frac{\epsilon_{11}^0}{\epsilon_{e11}^\infty} \left\{ \frac{A}{\lambda_1} [\exp(\lambda_1) - 1] + \frac{B}{\lambda_2} [\exp(\lambda_2) - 1] \right\}, \tag{C-5}$$

where

$$\lambda_1 = -\left(\tau_{11}^{-1} + \Delta\right)/2, \qquad \lambda_2 = -\left(\tau_{11}^{-1} - \Delta\right)/2, \tag{C-6}$$

with

$$\Delta = \frac{1}{\tau_{11}} \left[1 + 4 \left(\frac{\epsilon_{11}^0 - \epsilon_{11}^\infty}{\epsilon_{e11}^\infty} \right) \right]^{1/2}, \tag{C-7}$$

and

$$A = -\frac{1}{\Delta} \left(\frac{\partial e_{11}^n}{\partial t} - e_{11}^n \lambda_2 \right), \qquad B = \frac{1}{\Delta} \left(\frac{\partial e_{11}^n}{\partial t} - e_{11}^n \lambda_1 \right). \tag{C-8}$$

Similar equations are obtained for the (33) component. The intermediate vector

$$\mathbf{V}^* = \left[H_y^n, E_x^*, E_z^*, e_{11}^*, e_{33}^* \right]^\top \tag{C-9}$$

is the input for an explicit fourth-order Runge-Kutta algorithm that solves the nonstiff part of equation (57), to give the solution at time $(n+1)\, dt$. A similar partition algorithm for solving Biot's poroelastic equations was developed by Carcione and Quiroga-Goode (1994).